Molecular determinants of inhibition of UCP1-mediated respiratory uncoupling

Antoine Gagelin, Corentin Largeau, Sandrine Masscheleyn, Mathilde Piel, Daniel Calderón-Mora, Frédéric Bouillaud, Jérôme Hénin, Bruno Miroux

Molecular determinants of inhibition of UCP1-mediated respiratory uncoupling

Antoine Gagelin[a, c, 1], Corentin Largeau[a, b, c, 1], Sandrine Masscheleyn[b, c], Mathilde S. Piel[b, c], Daniel Calderon-Mora[b, c], Frédéric Bouillaud[d], Jérôme Hénin[* a, c], and Bruno Miroux[* b, c]

[a] *Université Paris Cité, Laboratoire de Biochimie Théorique CNRS UPR9080, Paris, 75005, France*
[b] *Université Paris Cité, Laboratoire de Biologie Physico-Chimique des Protéines Membranaires CNRS UMR7099, Paris, 75005, France*
[c] *Institut de Biologie Physico-Chimique, Fondation Edmond de Rothschild, Paris, 75005, France*
[d] *Université Paris Cité, Institut Cochin, Inserm U1016, CNRS UMR8104, Paris, 75014, France*
[1] *These authors contributed equally to this work*
[*] *These authors jointly supervised the work. Email: jerome.henin@cnrs.fr, bruno.miroux@ibpc.fr*

Abstract

Brown adipose tissue expresses uncoupling protein 1 (UCP1), a mitochondrial transporter that uncouples respiration from ATP synthesis and dissipates energy as heat, making it a target for treating obesity and related metabolic disorders. Here, we combine molecular dynamics simulations with mitochondrial respiration assays to investigate how purine nucleotides inhibit respiration uncoupling by UCP1. Simulations predict that GDP binds UCP1 in the common substrate binding site in an upright orientation, where the base moiety interacts with a pair of charged residues (R92/E191) that are specifically conserved in the subfamily of UCPs. E191, among others, interacts with purine but not pyrimidine bases, suggesting a rationale for nucleotide specificity in UCP1 inhibition. We also identify a triplet of uncharged residues involved in hydrophobic contacts with GDP. Site-directed mutagenesis of either I187 or W281 to alanine increases lauric acid-induced uncoupling activity of UCP1 and partially suppresses inhibition of UCP1 activity by GDP in yeast spheroplasts. The triple mutant (F88, I187, W281) to alanine is overactivated by lauric acid even in a high concentration of purine nucleotides. Variants at these positions may help increase energy expenditure in a cellular and therapeutic context.

Introduction

Uncoupling protein 1 (UCP1), a member of the SLC25 mitochondrial carrier family, is found in brown adipose tissue (BAT), an organ specialized in non-shivering thermogenesis in small mammals and some adult humans. UCP1 is abundant in the inner membrane of BAT mitochondria, where it dissipates the electrochemical proton gradient and thus uncouples respiration from ATP synthesis, which in turn increases respiration, reoxidation of coenzymes, substrate oxidation, and energy release as heat. UCP1 transports protons when activated by micromolar concentration of free fatty acids (FFAs) released by lipolysis of triglycerides [1].

Stimulating energy expenditure, as occurs in brown fat upon cold exposure, is an attractive approach for treating metabolic diseases such as obesity and diabetes. Adipocyte browning by expression of UCP1 has been successfully attempted in obese mice models and is a promising avenue for human therapy [2, 3]. However, increasing UCP1 levels in adipocyte mitochondria may not be sufficient to significantly modify energy balance and body mass in humans because, in basal conditions, wild-type UCP1 is inhibited by millimolar concentrations of purine nucleotides [1, 4]. This work aims to get molecular insight into UCP1 regulation and to design unregulated variants exhibiting enhanced uncoupling activity and less inhibition by nucleotides.

There is no experimentally resolved structure of UCP1. However, a general mechanism of transport by mitochondrial carriers has been proposed based on atomic structures of the related ADP/ATP carrier (AAC) [5]. In the C-state conformation of AAC induced by carboxyatractyloside (CATR) [6, 7], the cavity is widely open toward the cytoplasmic side, allowing ADP to enter the positively charged electrostatic funnel [8, 9]. Within the common substrate binding site located in the middle of the cavity, ADP is stabilized by electrostatic interactions with positively charged amino acids. This charged motif is supported by a matrix salt bridge and a highly conserved glutamine brace network at the C-terminus of odd α-helices [10]. In the matrix-facing M-state induced by bongkrekic acid (BKA) [11], the orientation of the cone-shaped protein is inverted upon the formation of a cytoplasmic salt bridge network found at the C-terminus of even helices. In the alternate access model, substrate binding drives the conformational changes required for the transition from C- to M-state, allowing a ping-pong-like mechanism of transport to occur.[5] Mitochondrial carriers exhibit an order-3 pseudo-symmetry due to an ancestral gene triplication [12]; as a result, their sequences can be analyzed based on symmetric or asymmetric sets of three paralogous residues (triplets) in the common substrate binding site [13, 7]. Like those of all members of the family, UCP1 sequences show highly-conserved consensus sequences involved in both salt bridge networks that are critical for the alternate access transport mechanism [10]. However,

it is still unclear how FFAs mediate proton transport in either UCP1 or AAC [14, 15] and how nucleotides, which are transported by AAC but not UCP1, inhibit UCP1 activity.

In this study, we build homology models of UCP1 in the two most likely putative conformations and perform molecular dynamics simulations with accelerated sampling methods to explore the accessibility and interactions of a GDP nucleotide within the UCP1 cavity. To experimentally confirm the predictions obtained from MD simulations, we express UCP1 wild-type and mutants in yeast and assess the respiratory response to activators and inhibitors. As a result, we identify unique molecular features of UCP1 that distinguish it from other mitochondrial carriers and find hyperactive UCP1 mutants that may be suitable for increasing energy expenditure in a therapeutic context.

Results

Structural models of UCP1

The structure with the closest sequence to UCP1 is one of UCP2 (58 % identity), which was obtained by liquid-state NMR [16] in the presence of DPC. This detergent perturbs the function and structure of AAC and UCP1 [17, 18, 19, 20, 21]. High-resolution crystal structures exist for the ATP/ADP Carrier (AAC), and AAC, like UCP1, has been shown to exhibit proton transport activity and to contribute to fatty-acid-dependent uncoupling of respiration [15]. Recently, AAC structures have been successfully used to model UCP2 [22].

Here, homology models of rat UCP1 were built based on AAC crystal structures in the C state [23] and M state [11], and for comparison, the NMR structure of UCP2 [16]. While multiple sequence alignments (MSAs) of a wider variety of homologous sequences were produced, they proved unnecessary for modeling due to the smaller MSA's lack of ambiguity. Figure 1a-b represents multiple sequence alignments between the three paralogous two-helix repeats within each sequence. This highlights major conserved features as well as a significant variation: helix 6 of the AAC sequence exhibits a deletion with respect to all other even-numbered helices at the position of UCP1 L278. The only case of manual adjustment of the alignments, at position L278, was not decided based on sequence information but rather on structural behavior in simulations (see Methods for details).

Because AAC sequences share only 20 % identity with rat UCP1, the homology models need to be carefully validated using external information. A model built using the automated machine-learned engine AlphaFold2 was analyzed for comparison. In addition, an independent homology model was built based on the recent cryo-EM structure of a putative mitochondrial carrier within mitochondrial complex IV of *Tetrahymena thermophila* [24].

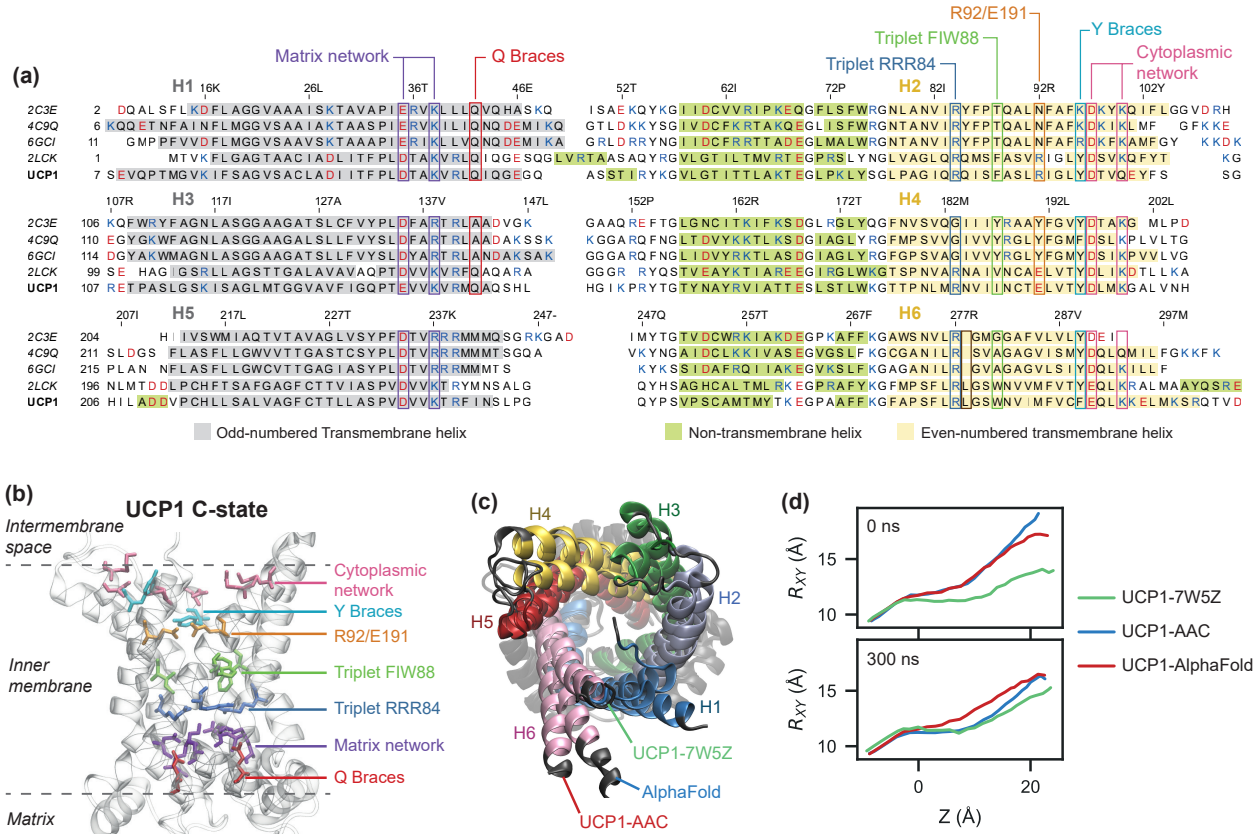

Figure 1: **UCP1 models tend toward a consensus apo C-state conformation.** **(a)** Multiple alignments of the sequences resolved in the structures of AAC (PDB 2C3E *Bos taurus*, PDB 4C9Q *Saccharomyces cerevisiae* and PDB 6GCI *Thermothelomyces thermophilus*), UCP2 (PDB 2LCK, *Mus musculus*) and *Rattus norvegicus* rUCP1. Residue numbers above the alignment refer to the UCP1 sequence. Colored backgrounds highlight α-helices detected in crystal structures of AAC and UCP2 and our C-state model of UCP1. **(b)** Cartoon representation of the UCP1 model based on AAC C-state, viewed from the membrane plane. **(c)** Overlapped cartoon representations of three rUCP1 models: based on AAC C-state, based on a putative C-state-like mitochondrial carrier in structure 7W5Z, and produced by AlphaFold. **(d)** Helix splay profiles along the transmembrane axis (Z axis) for three C-state-like models initially and after 300 ns relaxation by all-atom simulation in a membrane.

This new structure is a unique example of a putative mitochondrial carrier in a CATR-free native C-state conformation, with sequence identity to UCP1 comparable to AAC.

A global comparison of these models indicates variations in the splay of helices on the cytoplasmic side (Figure 1c), which tends to decrease upon physical relaxation in an all-atom MD simulation (Figure 1d), converging towards the least splayed variant, based on cryo-EM structure 7W5Z. We characterized the models by estimating their permeability to water in simulations (Figure S1). The NMR structure of UCP2 is known to be fully open

and water-permeable [17], and our model of UCP1 follows the same trend. In comparison, AAC structures and UCP1 models based thereon exhibit little or no permeability, and GDP binding further decreases the permeability of the C-state UCP1 model.

GDP preferentially binds C-state UCP1, in an upright orientation

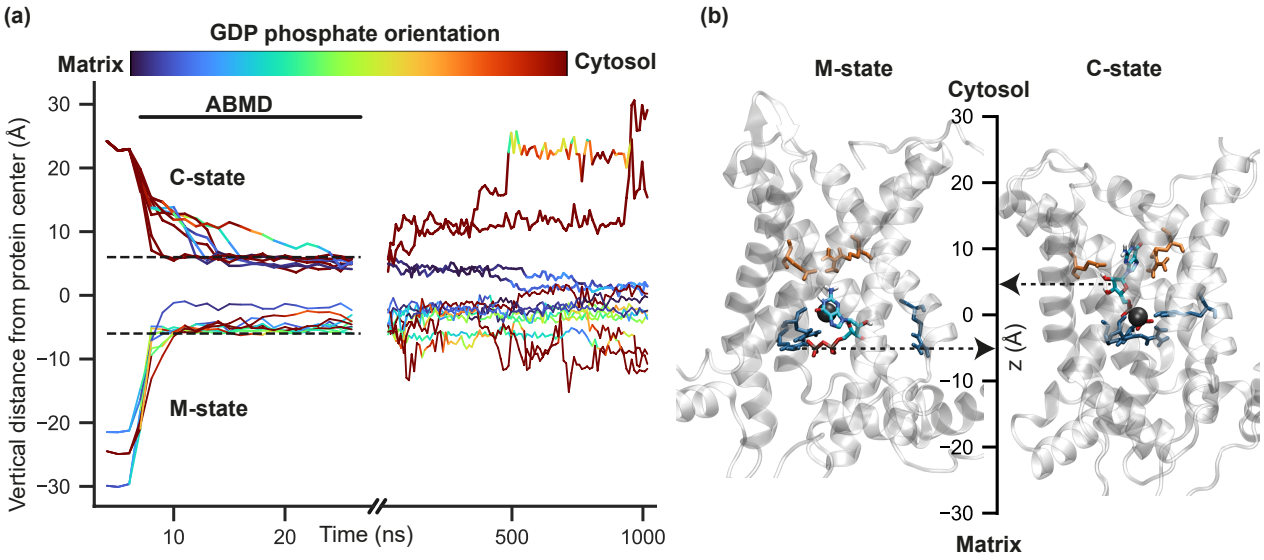

Figure 2: **Simulated binding pathways of GDP to UCP1 in the C-state and M-state conformations (a)** Vertical distance of GDP center of mass from the protein center (in Å) as a function of simulation time. Colors indicate GDP orientation, computed as the cosine of the angle between the phosphate-base vector of GDP and the z-axis. Binding was accelerated using the ABMD method for 20 ns followed by 1 µs unbiased relaxation. **(b)** Snapshots of UCP1 M-state (left) and C-state (right) with bound GDP. The center axis shows the vertical distance of GDP from the protein center (represented by a black sphere). UCP1 residues represented as sticks are R92-E191 (orange) and triplet RRR84 (blue).

Multiple trajectories of GDP binding were obtained from Adiabatic Bias Molecular Dynamics (ABMD) simulations. This method enables minimally biased, rapid sampling of GDP binding by selecting thermodynamic fluctuations of the nucleotide that favor binding. We explored binding to the cavity in both the C-state and the M-state models, in agreement with experimental evidence that UCP1 is accessible to ATP from both sides [25]. GDP was initially placed at the boundary between the intermembrane or matrix side and the UCP1 C-state and M-state models, respectively. The timelines of these trajectories are represented in Figure 2a. GDP entry in the M-state conformation is rapid and direct, with no preferential orientation of GDP and no obstacle until it reaches the center of the protein and forms contacts with triplet RRR84 (Figure 2b, left). In contrast, binding trajectories to the C-state conformation show much more structure. First, GDP tends to align along the transmembrane

axis, leading to two orientation modes with the phosphate group pointing either toward the protein center or towards the cytoplasm opening (line colors in Figure 2a). Second, some binding trajectories slow down around 11 Å from the protein center due to the presence of a salt bridge composed of R92 and E191 extending across the cavity and linking helix 2 with helix 4. Of note, this salt bridge was not present in any of the initial C-state models (homology or AlphaFold) but formed on the 100-ns timescale during the initial relaxation simulation, as helix splay on the cytoplasmic side relaxes (Figure 1d). Supporting Video S1 shows that GDP can either disrupt this salt bridge or bypass it (an entropic bottleneck) to reach the center. A subset of these trajectories was extended with 1 µs unbiased relaxation simulations to allow GDP to explore the cavity and to assess the final pose stability at each end-point. For the C-state conformation, two trajectories ending in each orientation of the phosphate group were selected for further relaxation. Only one of these orientations, with the diphosphate group facing the arginine triplet, is stable on the microsecond timescale, the phosphate group of GDP interacting with triplet RRR84 and the base moieties with residues F88 or W281 as well as R92 and E191 (Figure 2b, right). In trajectories where GDP binds in the opposite orientation, spontaneous unbinding is observed within 1 µs. In the M-state conformation, 1 µs unbiased relaxation trajectories confirm the absence of preferential orientation and broad distribution of positions of GDP within the cavity. In further extended simulations, GDP unbinds on the microsecond timescale in two out of three simulations (data not shown). Therefore, further analysis of GDP-UCP1 interactions was performed on the C-state only.

Molecular determinants controlling UCP1 inhibition

To obtain a more precise map of interactions of bound GDP with UCP1 C-state and account for possible effects of GDP binding on UCP1 conformation, simulations were run with the initial model bound to GDP from the onset in poses based on clustering analysis of the binding simulations. Respectively, three and four simulations were run for 2 µs for the *apo* and GDP-bound models.

Identification of a conserved pair of charged residues involved in GDP inhibition

Simulations of the *apo* C-state UCP1 model show the formation of the salt bridge between R92 and E191, which partially obstructs the cavity on the cytosolic side (Figure 3a-b), hence its effect on GDP binding trajectories. However, in the presence of GDP in the cavity, the R92-E191 salt bridge is significantly reduced (Figure 3a). Instead, strong interactions between the R92 and E191 residues and the nucleotide are observed (Figure 3c). To experimentally

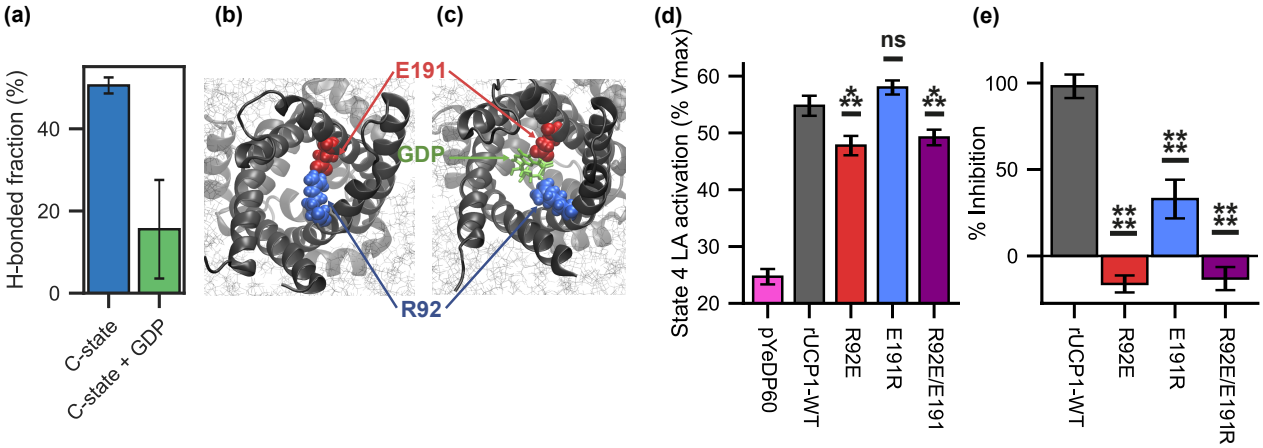

Figure 3: **UCP1-specific salt bridge across the cavity controls UCP1 inhibition by nucleotides. (a)** Bonded time of E191/R92 salt bridge as a fraction of simulation time. Average over the trajectories of the replicas, excluding the 200 first nanosecond of simulation. The error bar is the Standard Error of the Mean of simulation replicas. **(b)**, **(c)** Snapshots of the typical behavior of R92 and E191 in UCP1 C-state respectively without and with GDP. **(d-e)** Statistical analysis of UCP1-dependent activation of respiration **(d)** and its inhibition by GDP **(e)**. Number of independent experiments (n): pYeDP60 n = 5; rUCP1-WT n = 9; R92E n = 11; E191R n = 11; R92E/E191R n = 11. Statistical analyses are presented in Tables S3 and S4.

address the function of these interactions, UCP1 wild-type (WT) and UCP1 mutants were expressed in yeast mitochondria, and UCP1-mediated uncoupling of respiration was assayed. The following mutations were introduced in rat UCP1: R92E or E191R to prevent the salt bridge formation, and the charge-swap double mutation R92E/E191R to attempt the salt bridge restoration by charge inversion. Expression levels of all mutants were assessed by immunological detection of recombinant rUCP1 and endogenous VDAC (see Figure S2 and Table S1). Respiratory coupling ratios (RCR) of yeasts expressing rUCP1-WT or mutants displayed no significant difference (Table S2).

Spheroplasts expressing UCP1-R92E or UCP1-R92E/E191R show a significant decrease of lauric acid (LA)-induced activation of respiration to 45 % VO_{2max} while UCP1-E191R behaves as UCP1-WT (Figure 3d). In spheroplasts expressing UCP1-R92E and UCP1-R92E/E191R, GDP does not inhibit LA-induced respiration increase. In contrast, for the UCP1-E191R mutant, GDP partially inhibits (21 %) LA-induced respiration (Figure 3e, see Table S3 and Table S4 for statistical analysis).

Accordingly, single mutations of the salt bridge demonstrate both amino acids' function controlling UCP1 inhibition by nucleotides. Unexpectedly enough, charge inversion of the salt bridge does not restore the wild-type phenotype. However, this is explained by simulations of the UCP1-R92E/E191R model showing collective salt bridge reorganization. Consequently,

E92 establishes a stable salt bridge with arginine residues of triplet RRR84 at the expense of the E92-R191 salt bridge (Figure S3).

UCP1-nucleotide contacts obtained from simulations

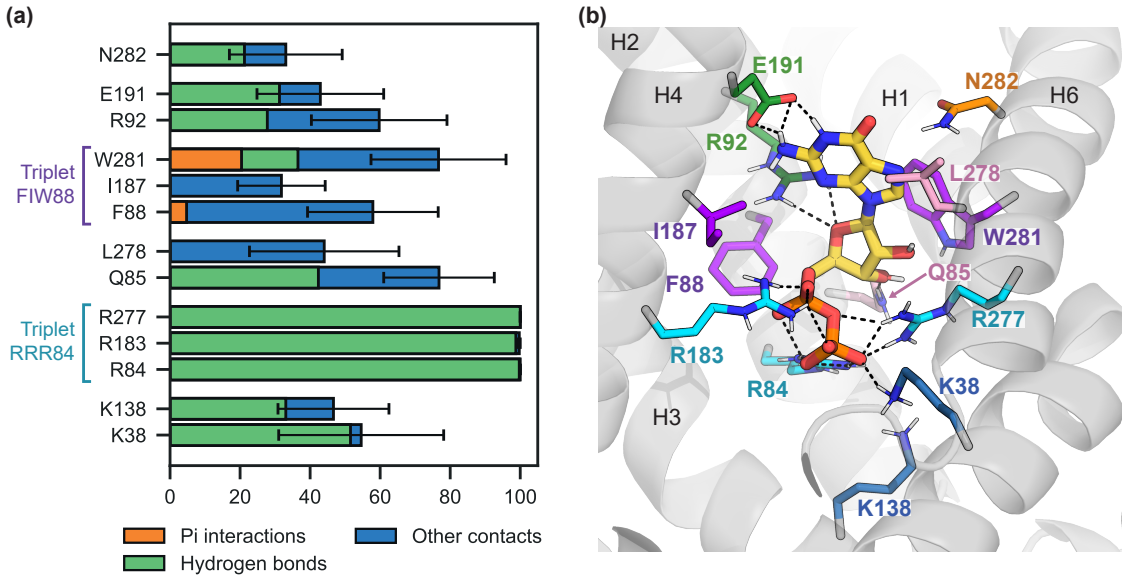

Figure 4: **Main interactions between GDP and UCP1 residues in simulations. (a)** Contact time between GDP and protein residues as a fraction of simulation time. The part of that contact time involving hydrogen bonds is represented in green, and the part involving pi interactions is represented in orange. Contact times are averaged over the trajectories, excluding the first 200 ns. The error bar is the Standard Error of the Mean between replicas. **(b)** Snapshot of the representative frame of the main GDP cluster (54 % of the frames, one out of three clusters). GDP is depicted as thick sticks with carbons in yellow. Protein residues are shown as thin sticks and are colored by triplets. Hydrogen bonds are represented as black dashed lines.

To get a comprehensive view of how GDP interacts with UCP1 within the common substrate binding site of mitochondrial carriers, we performed a statistical analysis of intermolecular contacts (Figure 4a). In addition, clustering was performed on GDP positions of MD simulations. The representative frame of the main cluster (54 % of the frames) is shown in Figure 4b. The nucleotide is anchored on two sides, with polar and non-polar interactions with the base and ribose moieties and five positively charged residues forming permanent or transient salt bridges with the phosphate group.

R92 and E191 have a high contact probability with GDP, E191 forms specific H bonds with the base of GDP, and R92 binds the phosphate group, the ribose, and the base alternatively. Residues of triplet FIW88 are engaged in frequent contact with the base or the ribose of GDP,

especially W281, which forms aromatic interactions ("pi stacking") with the purine base. The list of contacts also includes two residues from asymmetric triplet QNL85 [13, 10], Q85 and L278. Arginine residues from triplet RRR84 have the highest contact probability, and the phosphate group remains close to the triplet during the entire duration of the three replicas, indicating a strong interaction. Lysine residues from the salt bridge network on the matrix side (K38 and K138) are also involved in electrostatic interactions with the phosphate group.

Of note, interactions between GDP and phospholipids were observed in MD simulations. The phospholipids enter the cavity through the gaps between transmembrane helices and form hydrogen bonds with the base. Phospholipids bind the same GDP atoms as E191, which lowers the binding rate of this residue. This mainly occurs in one of the replicas, where a POPE molecule binds GDP during the whole simulation: this increases the observed variance of contact rates without affecting the list of contact residues.

Triplet FIW88 is critical for the control of UCP1 activity

Since triplet FIW88 also is in contact with GDP in simulations and is located between the R92/E191 pair and triplet RRR84, one helix turn away from both, we investigated its role in GDP inhibition of UCP1 activity by site-directed mutagenesis. The following apolar mutations were introduced in rat UCP1: FIW88AAA, F88A, I187A, and W281A. Expression levels of all mutants were assessed by immunodetection of both recombinant UCP1 and endogenous mitochondrial VDAC (Figure S2 and Table S1).

The superposition of the five curves shows three distinct phenotypes (Figure 5a). Spheroplasts expressing rUCP1-FIW88AAA exhibit an increase in respiration in response to LA and a complete loss of respiration inhibition by GDP. Decomposition of the triplet mutant in single mutation reveals that rUCP1-F88A has a respiration profile identical to rUCP1-WT. In contrast, rUCP1-I187A and rUCP1-W281A have increased respiration in response to LA and 75 % loss of respiration inhibition by GDP (Figure 5c and Tables S5 and S6 for statistical analysis). Simulations of the rUCP1-FIW88AAA mutant with bound GDP show a displacement of the base moiety of GDP and an increase in hydration of the site by about 8 water molecules compared with the wild-type. In particular, increased hydration points to a possible indirect role of I187 in GDP binding, whereby it limits the amount of water in the cavity, which would otherwise compete with GDP for polar interactions with the protein.

To illustrate the lack of regulation of the rUCP1-FIW88AAA mutant in a closer cellular context, GDP was added before LA. Figure 6 shows that, after inhibition of rUCP1-WT with GDP, the addition of LA hardly stimulates UCP1-mediated respiration uncoupling. In contrast, rUCP1-FIW88AAA rapidly increases respiration uncoupling in response to LA, even in the presence of GDP.

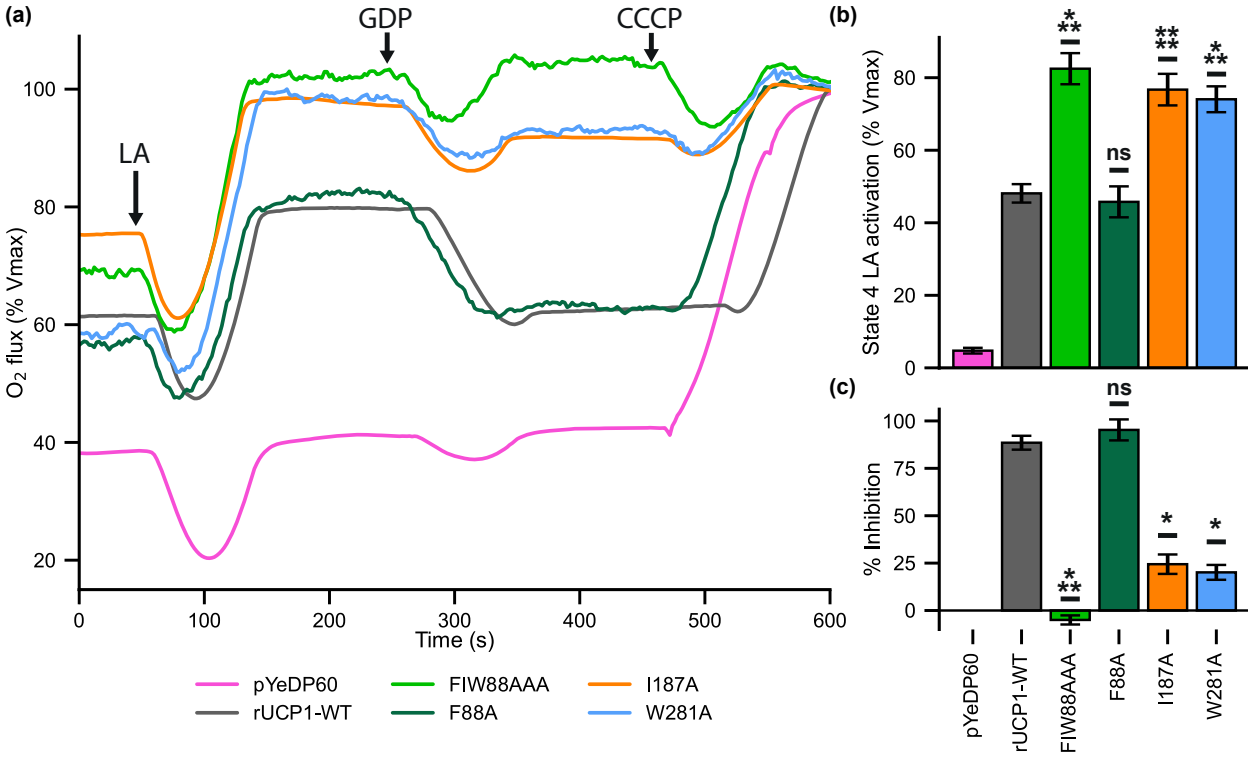

Figure 5: **Aromatic residues within the common substrate binding site control UCP1 regulation.** **(a)** Representative oxygen flux consumption curves of permeabilized spheroplasts harboring either plasmid expression rUCP1-WT or mutants. **(b)** UCP1 activation in response to LA. **(c)** Inhibition by GDP of UCP1-dependent increase of respiration after adding LA. Number of independent experiments (n): pYeDP60 n = 10; rUCP1-WT n = 11; FIW88AAA n = 11; F88A n = 11; I187A n = 11; W281A n = 11. Statistical analyses are presented in Tables S5 and S6.

Molecular bases for nucleotide specificity of UCP1 inhibition

It has been shown that pyrimidine nucleotides do not inhibit UCP1-mediated uncoupling of respiration [26]. As expected, UDP and GDP show similar contacts between the phosphate and ribose moieties and residues of the UCP1 cavity but not with the base moiety of UDP (Figure 7). UDP does not bind E191, W281, or Q85 but preferentially binds N184 and N188, which have little interaction with purine nucleotides. Thus, these three residues might be responsible for the selectivity of UCP1 inhibition by purine nucleotides.

Discussion

Here we have used UCP1 simulations and functional assays to explore how nucleotides inhibit UCP1 uncoupling activity. The convergence of structural models from different origins under simulation indicates that AAC-based models of UCP1 C-state are biased towards excessive

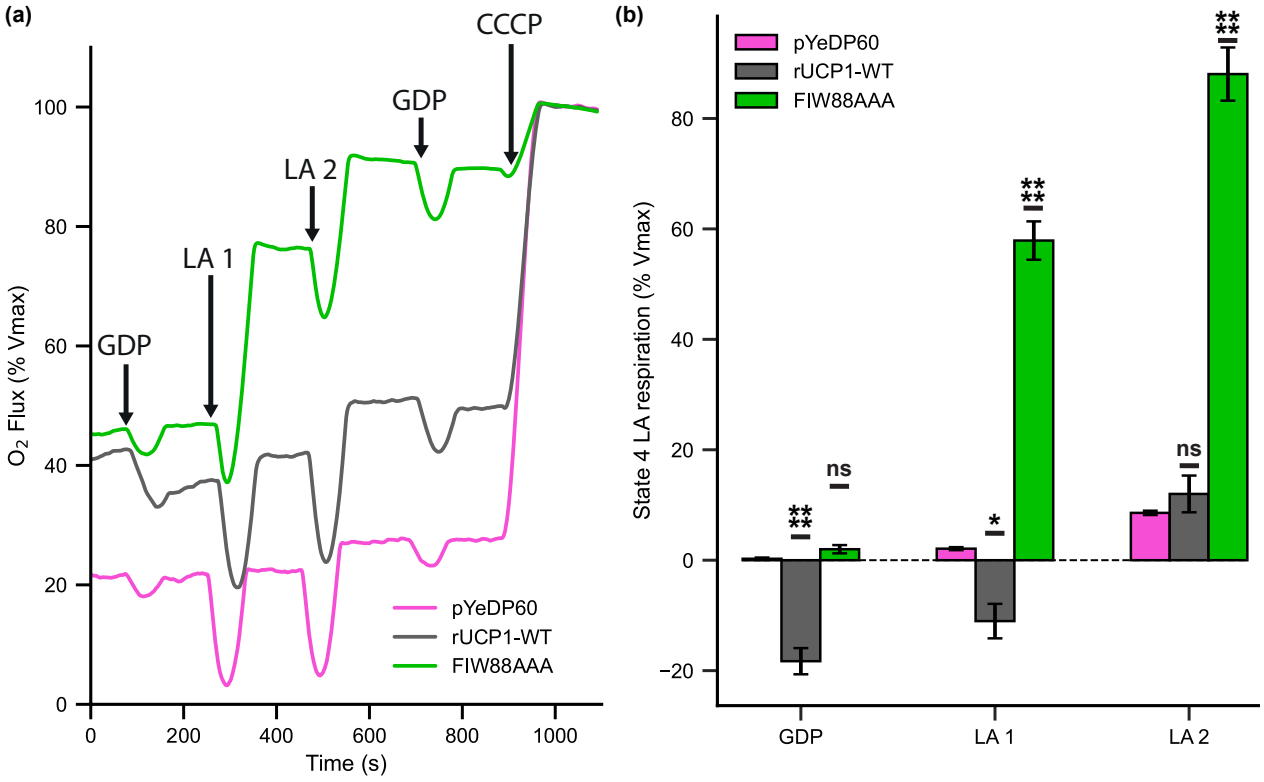

Figure 6: **rUCP1-FIW88AAA responds to LA and uncouples respiration in the presence of GDP.** **(a)** Experimental curves of permeabilized spheroplasts harboring either rUCP1-WT or rUCP1-FIW88AAA. Arrows represent the different injections. **(b)** Effect of GDP and of two lauric acid addition after GDP inhibition. Number of independent experiments (n): pYeDP60 n = 6; rUCP1-WT n = 11; FIW88AAA n = 11. Statistical analysis is presented in Table S7.

opening on the C side and that physics-based relaxation of UCP1 models tends to recover the native shape.

The SLC25 family of alpha-helical mitochondrial transporters is challenging to study *in vitro* because they are highly prone to inactivation by detergent [17, 27]. Therefore, we have chosen to assess predictions from molecular modeling directly by respiration assays of recombinant yeast spheroplasts to avoid the pitfall of inactivating UCP1 protein in detergent solution. Both computational and biochemical approaches converge toward a mechanism for UCP1 inhibition by GDP, in which interactions with residues R92 and E191 are critical.

R92 and E191 residues have been previously studied in the context of the pH dependence of UCP1 nucleotide binding. The R92T mutation lowers GTP affinity and completely abolishes the pH sensitivity of nucleotide binding to UCP1 [28] whereas E191Q only partially modifies this pH sensitivity, resulting in an increased GTP affinity at pH higher than 6.8 [29]. Martin Klingenberg postulated the existence of a salt bridge involving E191 acting

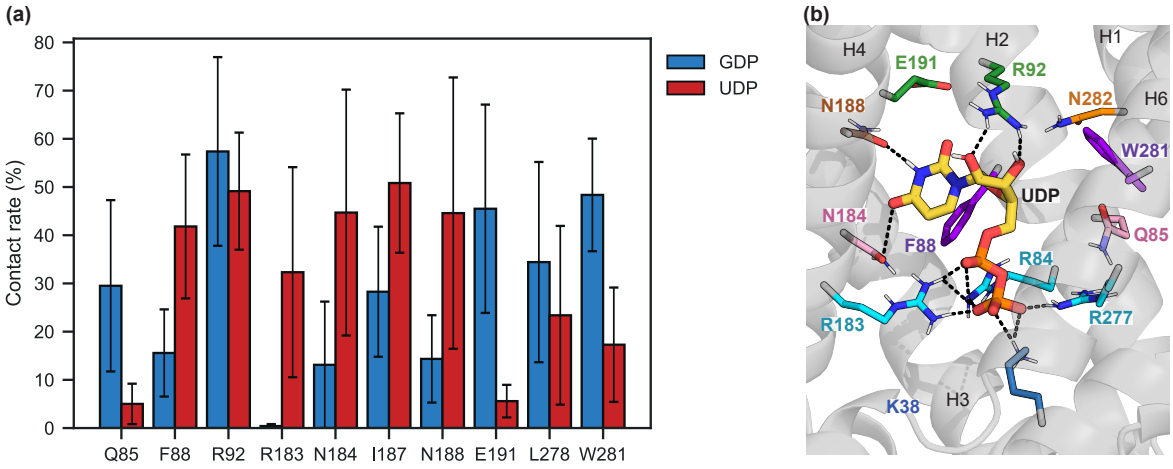

Figure 7: **UDP exhibits reduced binding to Q85, E191 and W281 in simulations.** **(a)** Contact times between nucleotide base and residues. Only the residues with the highest contact rate are represented. Contact times are averaged over the trajectories from 200 ns to 800 ns. The error bar is the Standard Error of the Mean between replicas. **(b)** Snapshot of the representative frame of the main UDP cluster (40 % of the frames, one out of three clusters). GDP is depicted as thick sticks with carbons in yellow. Protein residues are shown as thin sticks. Hydrogen bonds are represented as black dashed lines.

as a pH-dependent gate for nucleotide access [30]. Our numerical study confirms both the existence of this salt bridge and its interference with GDP binding. Analysis of simulated trajectories of GDP binding shows either disruption or bypass of the R92-E191 salt bridge to enter the cavity. Once GDP relaxes inside the binding site, the salt bridge dissociates, allowing R92 and E191 to interact directly with the nucleotide. Although charge inversion in the E92-R192 mutant did not restore the wild-type phenotype, MD simulations of this mutant show that charge inversion results in a reorganized network of salt bridges around R191, explaining the lack of phenotype restoration. Sequence alignment of mitochondrial carriers (Figure S4) shows that the R92-E191 salt bridge is almost uniquely restricted to the subfamily of UCPs (UCP1, UCP2, UCP3, UCP4, and UCP5). Only one other human mitochondrial carrier, SCMC1, which transports ATP-Mg^{2+} against phosphate, contains charged residues equivalent to R92/E191.

One helix-turn below R92 triplet, residues of the cavity-facing triplet FIW88, primarily F88 and W281, establish contacts with the base and ribose moiety of the nucleotide (Figure 4). W281, in particular, gives a strong signal both in experiments and simulations. The triplet mutation FIW88AAA in UCP1 not only suppresses GDP inhibition of respiration uncoupling but also exhibits an increased FFA-dependent respiration uncoupling activity, insensitive to the initial addition of GDP. Molecular dynamics simulations on AAC show the binding of the fatty acid via a fenestration between transmembrane helices 5 and 6, leading to water

molecules leaking across the membrane [31]. That work identified a specific contact between FFAs and AAC residue Y186 equivalent to I187 in UCP1. Given that both I187A and W281A single mutations enhance UCP1 uncoupling activity with a significant loss of inhibition by nucleotides (Figure 5b), and despite sequence and asymmetric differences between the two triplets (TYG in AAC, FIW88 in UCP1), these data support a competition model for both carriers between FA and the base moiety of purine nucleotides [32]. At the level of FIW88 triplet within the cavity of UCP1, LA and nucleotide would compete for interaction with both I187 and W281 residues. Of note, I187 and E191 residues are replaced by highly conserved Y186 and Y190 residues in AAC, which have been described as part of a tyrosine ladder by Pebay-Peyroula and colleagues [6].

At the end of the cavity, one helix-turn away from triplet FIW88, the phosphate moiety of nucleotide forms a stable interaction with triplet RRR84, which corresponds to triplet RGR88 of AAC also documented as a nucleotide anchor point [33, 34]. Similar interactions have been observed in simulations of ADP binding to AAC [8, 9] and UCP2 [22].

Our results complete previous knowledge to highlight differences between AAC and UCP1 with respect to nucleotide binding. Previous mutagenesis results on yeast AAC have highlighted several positively charged residues in the C-state cavity [35, 36], which are essential for AAC transport function and replaced by uncharged residues in the UCP1 sequence (Figure 1). In addition, UCP1 also lacks asymmetric triplets, which are critical for substrate selectivity within the common substrate binding site [13]. A critical example is the asymmetric triplet RGR83 in AAC, whose UCP counterpart is the symmetric triplet RRR84. All three arginines are known to be essential for UCP1 inhibition [37, 38, 28]: indeed, we find that the phosphate moiety of GDP consistently binds all three arginine residues (Figure 4). In contrast, in AAC, asymmetric placement of the two arginines determines an asymmetric position of the nucleotide [34, 8, 9]. In a recent conceptual model of nucleotide translocation by AAC, the small size of G199 leaves a gap that can accommodate the base moiety (Figure 2a in ref. [5]). This would allow the base to flip to the matrix side, which is expected to be necessary for transport [36]. Substitution of this glycine with R183 in UCP1 closes this gap and results in a much tighter ring of residues. We also find that additional interactions (mainly R92, E191, I187, and W281) stabilize GDP in an orientation orthogonal to the plane of triplet RRR84, further preventing any movement of the base towards the matrix side. Altogether, these differences provide a basis for explaining the lack of nucleotide transport by UCP1 as opposed to AAC.

Stimulating energy expenditure through respiratory uncoupling has been proposed in a therapeutic context for metabolic diseases [2, 3]. Search for UCP1-activating drugs other than FFAs has been attempted [39]. The drug will need to cross several barriers to reach the inner

mitochondrial membrane and overcome the natural inhibition of UCP1 by purine nucleotides. An alternative approach is to design unregulated variants of UCP1 to minimize the need for activating drugs or FFAs. In contrast to E191R and R92E, alanine variants of triplet FIW88 fulfill those criteria: they entirely escape nucleotide inhibition and display increased basal and FFAs-stimulated uncoupling activity in the cellular context of high nucleotide concentration. They may therefore represent a promising variant for adipocyte browning to stimulate energy metabolism in engineered human adipocytes.

Methods

Modeling and simulations

Structural models Homology models of rat UCP1 were based on two high-resolution X-ray crystal structures of AAC, one in a C-state conformation (*Bos taurus*, PDB entry 2C3E [23]) and the other in the M-state conformation (*Thermothelomyces thermophilus*, PDB entry 6GCI [11]). Sequences were aligned using MAFFT [40]. Two homology models were created using MODELLER [41] from the two AAC conformations. Some restraints on secondary structures were added in MODELLER at the termini of the protein (residues 7-14 and 296-301) to keep these parts of the protein in an α-helix configuration. Three cardiolipin molecules were placed around the models according to their positions in crystal structures of *Bos taurus* AAC. Three cardiolipin molecules partially modeled in crystal structures were kept and embedded in membranes with homology models (five cardiolipin molecules are partially resolved in the AAC M-state crystal structure but only three were kept in the initial model for consistency with the C-state model). The UCP1 C-state model created from the alignment of Figure 1 showed instabilities in helix 6 during relaxation simulations, resulting in loss of secondary structure around L278. L278 is an insertion in UCP sequences regarding AAC sequences, and MODELLER could not create a stable α-helix AAC C-state with a gap on L278. Manually removing the gap in the AAC sequence highly improves the stability of helix 6 in UCP1 C-state simulations. This results in a rotation of the end of the helix by 1/4 of the turn, yet this rotation relaxes during simulations without disrupting the helix. In contrast, M-state models were built using the original alignment because it yielded a stable helix 6 in simulations, whereas the helix rotation created when the gap was removed disrupted the salt bridge network on the cytosolic side, a key feature for the stability of the M-state.

As a control, a homology model of rat UCP1 based on the NMR structure of *Mus musculus* UCP2 [16] (PDB entry 2LCK) was produced. The whole UCP1 sequence was used to build

the model and three cardiolipin molecules were manually placed around the model at a similar position to that in the UCP1 C-state model.

The sequence of the putative mitochondrial carrier from the Cryo-EM structure 7W5Z chain M2 (Uniprot entry Q23M99) was aligned on rat UCP1 with MAFFT. After manual adjustments to the alignment, MODELLER was used to generate the UCP1-7W5Z model. The UCP1-AlphaFold model was retrieved from the AlphaFold Protein Structure Database.

Molecular dynamics simulations

Simulation setup Membrane-embedded, solvated simulation models of UCP1 *apo* M-state and C-state were built using CHARMM-GUI membrane builder [42]. 100×100 Å^2 membranes were built with the following composition: on the cytosolic side the leaf composition is 50 % POPC, 40 % POPE, and 10 % CL, on the matrix side the leaf composition is 40 % POPC, 30 % POPE and 30 % CL. The systems were assembled with a salinity of 150 mM of KCl and hydrated by around 14400 TIP3P [43] water molecules. Proteins were prepared with protonated lysine and arginine, neutral histidine and cysteine, and deprotonated glutamate and aspartate residues. CHARMM-GUI standard minimization and equilibration were used for the M-state model (total restrained equilibration time of 1.85 ns). Due to secondary structure instabilities on the 2nd helix of the UCP1 C-State model, the restrained equilibration time was extended to a total of 30.75 ns. After equilibration, the size of the simulation box is around $98 \times 98 \times 84$ Å^3 for C-state simulations and around $99 \times 99 \times 87$ Å^3 for M-state simulations. GDP was used as an inhibitor to match experimental conditions. Whenever GDP was included, it was modeled in the GDP^{3-} protonation state.

Molecular dynamics simulations All MD simulations were performed using the NAMD software [44] with the CHARMM36m force field [45] in the NPT ensemble at 310 K, 1.013 bar, and periodic boundary conditions. Underdamped Langevin dynamics with a coupling coefficient of 0.1 ps^{-1} was used to control temperature, without coupling for hydrogen atoms. Pressure was maintained using the Langevin piston algorithm with an oscillation period of 200 fs and a damping timescale of 100 fs.

All simulations used hydrogen mass repartitioning (HMR) [46] and a timestep of 4 fs. Three independent simulations of 2 µs were performed for UCP1 C-state *apo* and three independent simulations of 1 µs were performed for UCP1 M-state *apo*. Simulation trajectories were visualized with VMD [47].

Equilibration, and simulation of the UCP1-NMR model were performed using the same protocol as UCP1 M-state simulations. A single-replica, 1 µs simulation was performed.

AAC simulations were started from the X-ray structures (2C3E for the C-state and 6GCI

for the M-state). Residues from G253 to V256, which are not resolved in the 6GCI structure, were reconstructed with Modeller. System preparation and simulation protocols were identical to those of UCP1 M-state simulations. One replica of each model was simulated for 1 µs.

Accelerated binding simulations To explore possible GDP binding trajectories and poses, simulations were run wherein binding was accelerated by non-equilibrium biases following the Adiabatic Bias Molecular Dynamics (ABMD) method [48]. The Tcl-scripted implementation of ABMD in the Colvars Module [49] was used and can be found here: `https://github.com/Colvars/colvars/blob/master/colvartools/abmd.tcl`.

To prepare the starting points of ABMD simulations of GDP binding, GDP^{3-} was placed at the entrance of the UCP1 cavity in one position on the cytoplasmic side for C-state simulations and in three different positions on the matrix side for the M-state simulations.

ABMD was applied to the distance between the nucleotide and the protein center, with force constant 10 kcal/mol/Å^2 and a final restraint level of 6 Å from the protein center. The protein center was defined as the center of a set of 18 alpha carbons, of the A27 to I29 triplets (on odd-numbered helices) and the Q83 to Q85 triplets (on even-numbered helices). This included the arginine triplet RRR84. After 20 ns under ABMD bias, simulations were continued without any bias for a total of 1 µs to allow for free exploration of the cavity by GDP. Nine replicas were carried out for C-state and four for each starting position for M-state simulations. ABMD simulations started from an early iteration of the models, which included full-length N and C-termini and the initial alignment of helix 6 (see Homology Modeling above). These differences are not expected to affect the specific results on GDP binding to the central cavity of UCP1.

Equilibration with nucleotide Nucleotide molecules were embedded inside UCP1 C-state and M-state homology models before equilibration, according to the estimated positions from the clustering on ABMD simulations. Simulations were performed with the same protocol as the *apo* model simulations. Respectively, four and three independent simulations of 2 μs were performed for UCP1 C-state + GDP and UCP1 M-state + GDP. Three independent simulations of 0.8 μs were performed for UCP1 C-state + UDP.

UCP1 FIW88AAA simulations The final protein structures of three UCP1 C-state trajectories with GDP were mutated in UCP1 FIW88AAA after 1 μs of relaxation. Then, simulations were continued during 1 μs.

Analysis of simulation trajectories

Water permeability. Water permeability was estimated by counting the number of water molecules which went through the membrane inside or near the protein. To detect such permeation events, the membrane was split into three regions of equal thickness along the z axis. A permeation event was detected if a water molecule goes from one side of the membrane to the other, traveling through the three regions of the membrane and staying within 15 Å of the protein. This criterion eliminates false positives due to water molecules diffusing across periodic boundaries.

Helix splay profiles. The average alpha-carbon positions $\mathbf{r}_i$ of the transmembrane helices in the membrane plane (X, Y) were computed a running 12 Å-wide window. From these average positions, the helix splay profile is computed as an in-plane radius of gyration:

$$R_{XY}(z) = \sqrt{\frac{1}{N}\sum_{i}^{N} \mid \mathbf{r}_i(z) - \overline{\mathbf{r}}(z) \mid^2} \tag{1}$$

where z is the position of the window, N the number of transmembrane helices and $\overline{\mathbf{r}}$ the average of $\mathbf{r}_i$ over all helices.

Contact detection. A contact between two groups of atoms was detected if at least one pairwise distance between the atoms of the two groups is lower than 3 Å. A hydrogen bond was detected if the distance between donor and acceptor atoms was less than 3.3 Å and the angle donor/hydrogen/acceptor was higher than 140°. A pi interaction was detected if at least three atoms of an aromatic ring of a protein residue were closer than 3.8 Å to aromatic rings of the nucleotide. A salt bridge was defined as bonded if the two residues formed at least one hydrogen bond. Computation were performed with MDAnalysis [50, 51] and VMD [47]. Charts were rendered using Matplotlib [52] and Seaborn [53].

Clustering. Clustering of GDP positions was performed with either TTClust [54] or the scikit-learn library [55]. Nucleotide positions were clustered after alignment of the transmembrane helices using an agglomerative clustering followed by a K-Means clustering.

In vivo respiration assays

All reagents were purchased from Sigma-Aldrich unless specified in the text.

Mutagenesis and yeast transformation The pYeDP60 yeast expression vector harboring rat UCP1 gene with an N-terminal $(His)_8$-tag and a TEV cleavage site was previously validated for the functional expression of UCP1 in yeast mitochondria [18]. Mutagenesis by gene synthesis was performed by Twist Bioscience and UCP1 cDNA was subcloned in the pYeDP60 vector. Mutations in UCP1 were verified by DNA sequencing of the recombinant vector (Eurofins).

Yeast transformation was performed following the lithium acetate/single-stranded carrier DNA polyethylene glycol method [56]. In brief, *Saccharomyces cerevisiae* strain W303-GAL4 was grown overnight in YPDA medium (yeast extract 1 %, adenine sulfate 540 µM, peptone 2 % (BD Biosciences), glucose 2 %) at 30 °C under 200 rpm agitation. Preculture (500 µL) was harvested by centrifugation at 5000xg for 2 min and washed twice with TE buffer (Tris-HCl 10 mM pH 7.5, EDTA 1 mM). The yeast pellet was resuspended with the transformation mix (500 µL PEG4000 40 % (Fluka), LiOAc 100 mM, DMSO 774 µM, YeastMaker DNA carrier 50 µg (Takara Bio), supplemented with 1 µg of pYeDP60 vector). The mixture was carefully homogenized by up and down pipetting 30 times and by shaking for 15 min at room temperature. The suspension was submitted to heat shock for 15 min at 42 °C. Cells were centrifuged for 2 min at 1000xg and washed three times in TE buffer. Finally, pellets were resuspended with 90 µL of TE buffer and spread on an SDAA plate (yeast nitrogen base without amino acid 0.67 %, tryptophan 195 µM, agar 2 % (Sigma) and casamino acids 0.5 % (USBio)). Plates were incubated for three days at 30 °C.

UCP1 expression in yeast and spheroplasts preparation Yeast preculture was done overnight at 30 °C under 200 rpm agitation in S-lactate medium (lactate 2 %, yeast nitrogen base without amino acids 0.67 %, 0.1 % casamino acids, $(NH_4)_2SO_4$ 9 mM, KH_2PO_4 7.3 mM, tryptophan 98 µM, pH 4.5 adjusted with NaOH) supplemented with 0.1 % glucose. Preculture was diluted to $OD_{600nm} = 0.03$ in S-lactate medium final volume, supplemented with 0.1 % glucose, and yeast cells were grown for 20 hours at 30 °C under 200 rpm agitation. Medium was exchanged with a new S-lactate medium, supplemented with 1 % galactose to induce UCP1 expression, and cells were further grown for 4 hours. Yeast cells were harvested by centrifugation (5000xg for 10 min), washed in water, and resuspended (10 mL/g of wet yeast pellet) in SED buffer (sorbitol 1 M, EDTA 25 mM, and 1.4-dithiothreitol 50 mM). Cells were incubated for 10 minutes at room temperature, then washed with zymolyase buffer (sorbitol 1.2 M, KH_2PO_4/K_2HPO_4 20 mM, pH 7.4), and resuspended (10 mL/g of yeast cells) in zymolyase buffer supplemented with 0.5 mg/mL Zymolyase-20T (Amsbio). After 45 min incubation at 30 °C, the resulting spheroplasts were washed three times (1000xg centrifugation, 5 min) with respiration buffer (sorbitol 1 M, EDTA 0.5 mM, $MgSO_4$ 2 mM,

NaCl 1.7 mM, KH_2PO_4/K_2HPO_4 10 mM, Bovine Serum Albuvine fatty acids free 0.1 %, pH 6.8). Finally, spheroplasts are stored at 4 °C in a respiration buffer (2 mL/g) for a night.

Extraction of total yeast proteins and mitochondria preparation For mitochondria preparation, spheroplasts were broken using a Potter-Elvehjem grinder by moving up and down the pestle 15 times in TES buffer (10 mM Tris-HCl, 1 mM EDTA, 250 mM Sucrose, pH 7). After centrifugation (800xg for 10 min at 4 °C), the supernatant was centrifuged for 30 min at 11 000xg. The mitochondria pellet was resuspended with 100 µL of TES and quantified using the BCA method.

For total yeasts proteins extracts, yeasts were grown according to the previous paragraph in S-Lactate with 4 hours of induction with 1 % galactose. A volume of culture corresponding to an $OD_{600nm} = 5$ was harvested by centrifugation (5000xg, 10 min) and washed with 500 µL of cold water. The supernatant was discarded before adding 400 µL of cold 5 % TCA (Trichloroacetic acid). Glass beads were added until reaching the meniscus. Yeasts were broken using MP Biomedicals FastPrep-24 during 4×20 s, chilling tubes on ice between vortexing to keep cells chilled. The supernatant was collected and beads were washed three times with 400 µL cold TCA. All supernatants were pooled and chilled on ice for 30 min. Proteins were pelleted by centrifugation at 16 000xg for 30 min at 4 °C. Pellets were resuspended with 100 µL of 100 mM Tris-HCl pH 7.5.

Immunodetection of UCP1 To ensure the equivalent expression level among all mutants and all biological replicates, 10 µL (equivalent to $OD_{600nm} = 0.5$) TCA extracts of total yeast or 2 µg of mitochondrial proteins were loaded on a 12 % SDS-PAGE and transferred onto a nitrocellulose membrane (GE Healthcare). UCP1 was detected using a mouse anti-pentahistidine tag:HRP 0.2 µL/mL (MCA5995P – Bio-RAD). VDAC1 Porin was used as a mitochondrial loading control and detected by a mouse anti-VDAC1 0.1 µL/mL (16G9E6BC4 - Invitrogen) and a goat anti-mouse tag: HRP 0.1 µL/mL (W402B - Promega).

Respiration measurements To assess UCP1 activity, O_2 consumption measurements were performed using an Oroboros instrument at 28 °C under 750 rpm agitation. Spheroplasts (2.5 mg/mL in respiration buffer with 250 µg/mL nystatin) were permeabilized for 15 min at 28 °C. Before the UCP1 activity measurement, the respiratory control ratio (RCR) was measured by successive addition of NADH (3.125 mM), ADP (0.625 mM), oligomycin (1 µM), and carbonyl cyanide m-chlorophenyl hydrazone (CCCP, 10 µM).

FFAs trigger proton leak activity in several mitochondrial carriers, especially in AAC [14, 15]), which is highly expressed in yeast mitochondria. We searched for LA concentration that

selectively stimulates UCP1-dependent uncoupling of respiration with no effect on AAC. Above 120 micromolar concentration, LA stimulates uncoupling of respiration in control yeast spheroplasts. The addition of CATR inhibits this increase in respiration showing that the main target of LA is yeast AAC (SI Figure S5a). The 60 micromolar concentration corresponding to the ratio LA/BSA = 4 was selected to stimulate UCP1 activity in yeast recombinant spheroplasts. At this concentration of LA, CATR does not affect respiration, showing that endogenous yeast AAC does not contribute to the LA-induced proton leak (Figure S5). As previously observed [18], this ratio LA/BSA = 4, does not affect control spheroplasts' respiration. In contrast, it significantly increases the respiration of spheroplasts harboring UCP1 to 55 % of maximal respiration rate (VO_{2max}) (see Figure S6 and Figure 3d).

The RCR was calculated by dividing the mean O_2-ADP flux by the mean O_2-oligomycin flux. RCR determination was performed with each independent yeast culture. UCP1 activity and inhibition were measured according to the following sequence: oligomycin (1 µM), NADH (3.125 mM), lauric acid (60 µM, corresponding to a ratio fatty acid/BSA = 4), GDP (1.25 mM), CCCP (10 µM). GDP was chosen over ADP or ATP to minimize artefacts due to transport by endogenous AAC in yeast. Mean O_2 fluxes were calculated from respiration curves with DatLab Oroboros software after each addition with a time window of 1 min. Data are presented as mean ± SEM (Standard Error of the Mean). For interpretation purposes, data were normalized by O_2-CCCP flux (F_{CCCP}) after removing O_2-NADH or by calculating the inhibition rate with $1 - \dfrac{F_{\mathrm{GDP}} - F_{\mathrm{NADH}}}{F_{\mathrm{AL}} - F_{\mathrm{NADH}}}$. Significant differences are assessed based on a One-way ANOVA and Donnett's multiple comparison test with rUCP1-WT, done on GraphPad PRISM (ns = not significant, $*$ = p-value ≤ 0.05, $**$ = p ≤ 0.01, $***$ = p-value ≤ 0.001, $****$ = p-value ≤ 0.0001).

Acknowledgments

The authors acknowledge support from ANR through LABEX DYNAMO (ANR-11-LABX-0011) and Equipex CACSICE (ANR-11-EQPX-0008) for the visualization wall, and from the Laboratoire International Associé of CNRS and UIUC. We are grateful to François Dehez and Christophe Chipot for stimulating discussions and Céline Ransy for help with respiration assays. AG and CL are supported by a French Ministry of Research and Technology PhD fellowship. This work was performed using HPC resources from GENCI-CINES (Grant A0100710760) and the LBT-HPC cluster managed by Geoffrey Letessier.

Author contributions

All authors designed the experiments and analyzed the data. AG, CL, SM, MP, and DCM performed the experiments. AG, CL, JH and BM wrote the paper with contributions from all authors.

Data availability

All data necessary for reproducing simulation results are available through Zenodo (DOI: 10.5281/zenodo.6337947)

References

[1] Nicholls, D. G. Mitochondrial proton leaks and uncoupling proteins. *Biochimica et Biophysica Acta (BBA) - Bioenergetics* **1862**, 148428 (2021). URL `http://www.sciencedirect.com/science/article/pii/S000527282100061X`. Publisher: Elsevier.

[2] Tsagkaraki, E. *et al.* CRISPR-enhanced human adipocyte browning as cell therapy for metabolic disease. *Nature Communications* **12**, 6931 (2021). URL `https://www.nature.com/articles/s41467-021-27190-y`. Number: 1 Publisher: Nature Publishing Group.

[3] Wang, C.-H. *et al.* CRISPR-engineered human brown-like adipocytes prevent diet-induced obesity and ameliorate metabolic syndrome in mice. *Science Translational Medicine* **12** (2020). URL `https://www.science.org/doi/abs/10.1126/scitranslmed.aaz8664`. Publisher: American Association for the Advancement of Science.

[4] Traut, T. W. Physiological concentrations of purines and pyrimidines. *Mol Cell Biochem* **140**, 1–22 (1994). URL `https://doi.org/10.1007/BF00928361`.

[5] Ruprecht, J. J. & Kunji, E. R. S. Structural Mechanism of Transport of Mitochondrial Carriers. *Annual Review of Biochemistry* **90**, 535–558 (2021).

[6] Pebay-Peyroula, E. Structure of mitochondrial ADP/ATP carrier in complex with carboxyatractyloside. *Nature* **426**, 8 (2003).

[7] Ruprecht, J. J. *et al.* Structures of yeast mitochondrial ADP/ATP carriers support a domain-based alternating-access transport mechanism. *Proceedings of the National*

Academy of Sciences **111**, E426–E434 (2014). URL http://www.pnas.org/cgi/doi/10.1073/pnas.1320692111.

[8] Dehez, F., Pebay-Peyroula, E. & Chipot, C. Binding of ADP in the mitochondrial ADP/ATP carrier is driven by an electrostatic funnel. *Journal of the American Chemical Society* **130**, 12725–12733 (2008). URL https://doi.org/10.1021/ja8033087.

[9] Wang, Y. & Tajkhorshid, E. Electrostatic funneling of substrate in mitochondrial inner membrane carriers. *Proceedings of the National Academy of Sciences* **105**, 9598–9603 (2008). URL http://www.pnas.org/cgi/doi/10.1073/pnas.0801786105.

[10] Crichton, P. G., Lee, Y. & Kunji, E. R. The molecular features of uncoupling protein 1 support a conventional mitochondrial carrier-like mechanism. *Biochimie* **134**, 35–50 (2017). URL https://linkinghub.elsevier.com/retrieve/pii/S0300908416303935.

[11] Ruprecht, J. J. *et al.* The Molecular Mechanism of Transport by the Mitochondrial ADP/ATP Carrier. *Cell* **176**, 435–447.e15 (2019). URL http://www.sciencedirect.com/science/article/pii/S0092867418315174.

[12] Saraste, M. & Walker, J. E. Internal sequence repeats and the path of polypeptide in mitochondrial ADP/ATP translocase. *FEBS letters* **144**, 250–254 (1982).

[13] Robinson, A. J., Overy, C. & Kunji, E. R. S. The mechanism of transport by mitochondrial carriers based on analysis of symmetry. *Proceedings of the National Academy of Sciences* **105**, 17766–17771 (2008). URL https://www.pnas.org/content/105/46/17766.

[14] Skulachev, V. P. Fatty acid circuit as a physiological mechanism of uncoupling of oxidative phosphorylation. *FEBS Letters* **294**, 158–162 (1991). URL https://onlinelibrary.wiley.com/doi/abs/10.1016/0014-5793%2891%2980658-P. _eprint: https://onlinelibrary.wiley.com/doi/pdf/10.1016/0014-5793%2891%2980658-P.

[15] Bertholet, A. M. *et al.* H+ transport is an integral function of the mitochondrial ADP/ATP carrier. *Nature* **571**, 515–520 (2019).

[16] Berardi, M. J., Shih, W. M., Harrison, S. C. & Chou, J. J. Mitochondrial uncoupling protein 2 structure determined by NMR molecular fragment searching. *Nature* **476**, 109–113 (2011). URL http://www.nature.com/articles/nature10257.

[17] Zoonens, M. *et al.* Dangerous Liaisons between Detergents and Membrane Proteins. The Case of Mitochondrial Uncoupling Protein 2. *Journal of the American Chemical Society* **135**, 15174–15182 (2013). URL https://pubs.acs.org/doi/10.1021/ja407424v.

582 [18] Piel, M. S., Masscheleyn, S., Bouillaud, F., Moncoq, K. & Miroux, B. Structural models
583 of mitochondrial uncoupling proteins obtained in DPC micelles are not functionally
584 relevant. *The FEBS journal* **288** (2020).

585 [19] Chipot, C. *et al.* Perturbations of Native Membrane Protein Structure in Alkyl Phos-
586 phocholine Detergents: A Critical Assessment of NMR and Biophysical Studies. *Chem-*
587 *ical Reviews* **118**, 3559–3607 (2018). URL `https://www.ncbi.nlm.nih.gov/pmc/`
588 `articles/PMC5896743/`.

589 [20] Kurauskas, V. *et al.* Dynamics and interactions of AAC3 in DPC are not functionally
590 relevant. *Nature Structural & Molecular Biology* **25**, 745–747 (2018).

591 [21] King, M. S., Crichton, P. G., Ruprecht, J. J. & Kunji, E. R. S. Concerns with yeast
592 mitochondrial ADP/ATP carrier's integrity in DPC. *Nature Structural & Molecular*
593 *Biology* **25**, 747–749 (2018).

594 [22] Škulj, S., Brkljača, Z., Kreiter, J., Pohl, E. E. & Vazdar, M. Molecular Dynamics
595 Simulations of Mitochondrial Uncoupling Protein 2. *International Journal of Molec-*
596 *ular Sciences* **22**, 1214 (2021). URL `https://www.mdpi.com/1422-0067/22/3/1214`.
597 Number: 3 Publisher: Multidisciplinary Digital Publishing Institute.

598 [23] Nury, H. *et al.* Structural basis for lipid-mediated interactions between mitochondrial
599 ADP/ATP carrier monomers. *FEBS Letters* **579**, 6031–6036 (2005). URL `http://doi.`
600 `wiley.com/10.1016/j.febslet.2005.09.061`.

601 [24] Zhou, L., Maldonado, M., Padavannil, A., Guo, F. & Letts, J. A. Structures of *Tetrahy-*
602 *mena* 's respiratory chain reveal the diversity of eukaryotic core metabolism. *Sci-*
603 *ence* **376**, 831–839 (2022). URL `https://www.science.org/doi/10.1126/science.`
604 `abn7747`.

605 [25] Zhu, R. *et al.* Mapping the nucleotide binding site of uncoupling protein 1 using atomic
606 force microscopy. *J. Am. Chem. Soc.* **135**, 3640–3646 (2013). `23414455`.

607 [26] Heaton, G. M. & Nicholls, D. G. The Structural Specificity of the Nucleotide-Binding
608 Site and the Reversible Nature of the Inhibition of Proton Conductance Induced by
609 Bound Nucleotides in Brown-Adipose-Tissue Mitochondria. *Biochemical Society Trans-*
610 *actions* **5**, 210–212 (1977). URL `https://portlandpress.com/biochemsoctrans/`
611 `article/5/1/210/89071/The-Structural-Specificity-of-the`.

[27] Dehez, F., Schanda, P., King, M. S., Kunji, E. R. & Chipot, C. Mitochondrial ADP/ATP carrier in dodecylphosphocholine binds cardiolipins with non-native affinity. *Biophysical Journal* **113**, 2311–2315 (2017). URL https://doi.org/10.1016/j.bpj.2017.09.019.

[28] Echtay, K. S., Bienengraeber, M. & Klingenberg, M. Role of Intrahelical Arginine Residues in Functional Properties of Uncoupling Protein (UCP1) †. *Biochemistry* **40**, 5243–5248 (2001). URL https://pubs.acs.org/doi/10.1021/bi002130q.

[29] Echtay, K. S., Bienengraeber, M. & Klingenberg, M. Mutagenesis of the Uncoupling Protein of Brown Adipose Tissue. Neutralization of E190 Largely Abolishes pH Control of Nucleotide Binding †. *Biochemistry* **36**, 8253–8260 (1997). URL https://pubs.acs.org/doi/10.1021/bi970513r.

[30] Klingenberg, M. UCP1 - A sophisticated energy valve. *Biochimie* **134**, 19–27 (2017). URL https://linkinghub.elsevier.com/retrieve/pii/S0300908416302966.

[31] Bertholet, A. M. *et al.* Mitochondrial uncouplers induce proton leak by activating AAC and UCP1. *Nature* (2022). URL https://www.nature.com/articles/s41586-022-04747-5.

[32] Shabalina, I. G., Jacobsson, A., Cannon, B. & Nedergaard, J. Native UCP1 Displays Simple Competitive Kinetics between the Regulators Purine Nucleotides and Fatty Acids. *Journal of Biological Chemistry* **279**, 38236–38248 (2004). URL http://www.jbc.org/lookup/doi/10.1074/jbc.M402375200.

[33] Kunji, E. R. S. & Robinson, A. J. The conserved substrate binding site of mitochondrial carriers. *Biochimica et Biophysica Acta (BBA) - Bioenergetics* **1757**, 1237–1248 (2006). URL https://www.sciencedirect.com/science/article/pii/S0005272806000764.

[34] Robinson, A. J. & Kunji, E. R. S. Mitochondrial carriers in the cytoplasmic state have a common substrate binding site. *Proceedings of the National Academy of Sciences* **103**, 2617–2622 (2006). URL http://www.pnas.org/cgi/doi/10.1073/pnas.0509994103.

[35] Nelson, D. R., Lawson, J. E., Klingenberg, M. & Douglas, M. G. Site-directed Mutagenesis of the Yeast Mitochondrial ADP/ATP Translocator: Six Arginines and One Lysine are Essential. *Journal of Molecular Biology* **230**, 1159–1170 (1993). URL http://www.sciencedirect.com/science/article/pii/S0022283683712337.

[36] Mavridou, V. *et al.* Substrate binding in the mitochondrial ADP/ATP carrier is a step-wise process guiding the structural changes in the transport cycle. *Na-*

ture Communications **13**, 3585 (2022). URL https://www.nature.com/articles/s41467-022-31366-5. Number: 1 Publisher: Nature Publishing Group.

[37] Murdza-Inglis, D. L. *et al.* A single mutation in uncoupling protein of rat brown adipose tissue mitochondria abolishes GDP sensitivity of H+ transport. *J. Biol. Chem.* **269**, 7435–7438 (1994). 8125963.

[38] Modrianský, M., Murdza-Inglis, D. L., Patel, H. V., Freeman, K. B. & Garlid, K. D. Identification by site-directed mutagenesis of three arginines in uncoupling protein that are essential for nucleotide binding and inhibition. *The Journal of Biological Chemistry* **272**, 24759–24762 (1997).

[39] Cavalieri, R. *et al.* Activating ligands of Uncoupling protein 1 identified by rapid membrane protein thermostability shift analysis. *Molecular Metabolism* **62**, 101526 (2022). URL https://linkinghub.elsevier.com/retrieve/pii/S2212877822000953.

[40] Katoh, K. MAFFT: a novel method for rapid multiple sequence alignment based on fast Fourier transform. *Nucleic Acids Research* **30**, 3059–3066 (2002). URL https://academic.oup.com/nar/article-lookup/doi/10.1093/nar/gkf436.

[41] Šali, A. & Blundell, T. L. Comparative Protein Modelling by Satisfaction of Spatial Restraints. *Journal of Molecular Biology* **234**, 779–815 (1993). URL https://linkinghub.elsevier.com/retrieve/pii/S0022283683716268.

[42] Jo, S., Kim, T., Iyer, V. G. & Im, W. CHARMM-GUI: A web-based graphical user interface for CHARMM. *Journal of Computational Chemistry* **29**, 1859–1865 (2008). URL https://onlinelibrary.wiley.com/doi/abs/10.1002/jcc.20945.

[43] Jorgensen, W. L., Chandrasekhar, J., Madura, J. D., Impey, R. W. & Klein, M. L. Comparison of simple potential functions for simulating liquid water. *The Journal of Chemical Physics* **79**, 926–935 (1983). URL http://aip.scitation.org/doi/10.1063/1.445869.

[44] Phillips, J. C. *et al.* Scalable molecular dynamics on CPU and GPU architectures with NAMD. *The Journal of Chemical Physics* **153**, 044130 (2020). URL http://aip.scitation.org/doi/10.1063/5.0014475.

[45] Huang, J. *et al.* CHARMM36m: an improved force field for folded and intrinsically disordered proteins. *Nature Methods* **14**, 71–73 (2017). URL http://www.nature.com/articles/nmeth.4067.

[46] Feenstra, K. A., Hess, B. & Berendsen, H. J. C. Improving efficiency of large time-scale molecular dynamics simulations of hydrogen-rich systems. *Journal of Computational Chemistry* **20**, 786–798 (1999). URL https://onlinelibrary.wiley.com/doi/10.1002/(SICI)1096-987X(199906)20:8<786::AID-JCC5>3.0.CO;2-B.

[47] Humphrey, W., Dalke, A. & Schulten, K. VMD: Visual molecular dynamics. *Journal of Molecular Graphics* **14**, 33–38 (1996). URL https://linkinghub.elsevier.com/retrieve/pii/0263785596000185.

[48] Marchi, M. & Ballone, P. Adiabatic bias molecular dynamics: A method to navigate the conformational space of complex molecular systems. *The Journal of Chemical Physics* **110**, 3697–3702 (1999). URL http://aip.scitation.org/doi/10.1063/1.478259.

[49] Fiorin, G., Klein, M. L. & Hénin, J. Using collective variables to drive molecular dynamics simulations. *Mol. Phys.* **111**, 3345–3362 (2013). URL http://www.tandfonline.com/doi/abs/10.1080/00268976.2013.813594. http://www.tandfonline.com/doi/pdf/10.1080/00268976.2013.813594.

[50] Michaud-Agrawal, N., Denning, E. J., Woolf, T. B. & Beckstein, O. MDAnalysis: A toolkit for the analysis of molecular dynamics simulations. *Journal of Computational Chemistry* **32**, 2319–2327 (2011). URL https://onlinelibrary.wiley.com/doi/10.1002/jcc.21787.

[51] Gowers, R. J. *et al.* MDAnalysis: A python package for the rapid analysis of molecular dynamics simulations. In Benthall, S. & Rostrup, S. (eds.) *Proceedings of the 15th Python in Science Conference*, 98 – 105 (2016).

[52] Hunter, J. D. Matplotlib: A 2D Graphics Environment. *Computing in Science & Engineering* **9**, 90–95 (2007). URL http://ieeexplore.ieee.org/document/4160265/.

[53] Waskom, M. seaborn: statistical data visualization. *Journal of Open Source Software* **6**, 3021 (2021). URL https://joss.theoj.org/papers/10.21105/joss.03021.

[54] Tubiana, T., Carvaillo, J.-C., Boulard, Y. & Bressanelli, S. TTClust: A Versatile Molecular Simulation Trajectory Clustering Program with Graphical Summaries. *Journal of Chemical Information and Modeling* **58**, 2178–2182 (2018). URL https://pubs.acs.org/doi/10.1021/acs.jcim.8b00512.

[55] Pedregosa, F. *et al.* Scikit-learn: Machine Learning in Python. *Journal of Machine Learning Research* **12**, 2825–2830 (2011).

[56] Daniel Gietz, R. & Woods, R. A. Transformation of yeast by lithium acetate/single-stranded carrier DNA/polyethylene glycol method. In Guthrie, C. & Fink, G. R. (eds.) *Methods in Enzymology*, vol. 350 of *Guide to Yeast Genetics and Molecular and Cell Biology - Part B*, 87–96 (Academic Press, 2002). URL `https://www.sciencedirect.com/science/article/pii/S0076687902509575`.